J. Fluid Mech. (1995), *vol.* 291, *pp.* 33–56

Multiple equilibria and stable oscillations in thermosolutal convection at small aspect ratio

By CHARLES QUON[1,2] AND MICHAEL GHIL[1]

[1] Climate Dynamics Center, Department of Atmospheric Sciences and Institute of Geophysics and Planetary Physics, University of California, Los Angeles, CA 90095-1565, USA

[2] Department of Fisheries and Oceans, Bedford Institute of Oceanography, Dartmouth, Nova Scotia, Canada

(Received 9 January 1994 and in revised form 14 October 1994)

For thermosolutal convection in an enclosure of arbitrary vertical aspect ratio, mixed boundary conditions – with salt flux and temperature prescribed on a horizontal boundary – can lead to symmetry breaking via pitchfork bifurcation. In the present paper we consider an enclosure of very small height-to-length aspect ratio δ, as encountered in the world's oceans. In this case, if the ratios of the vertical to horizontal components of viscosity, $\mathscr{P}$, and of diffusivity, $\mathscr{Q}$, are of order unity, advective transport cannot set in even at very high Rayleigh numbers. The ratios $\mathscr{P}$ and $\mathscr{Q}$ must be substantially less than unity in order for convection to dominate the heat and solute transport.

We have investigated numerically the effects of monotonic and non-monotonic temperature and salinity boundary conditions in a two-dimensional domain at constant $\delta = 0.01$ and constant $\mathscr{P} = \mathscr{Q} = 0.01$. This ratio of eddy-mixing coefficients reflects the different scales of motion – vertical and horizontal – in the ocean, rather than a physically realizable laboratory fluid. It is found that when the salt-flux strength, γ, is sufficiently large, the system undergoes a second bifurcation for both types of boundary conditions. It is a Hopf bifurcation, leading from the asymmetric steady states produced by the first one to oscillatory solutions. These periodic solutions are stable and very robust. An approximate Hopf bifurcation diagram has been produced. We conclude that non-monotonic salt-flux conditions are neither necessary nor sufficient to induce the oscillations, while the strength of the salt flux is crucial.

1. Introduction

The possibility of multiple equilibria – symmetric or antisymmetric, temperature- or salinity-driven – in the oceans's circulation has been raised by Stommel (1961) in a two-box model. The problem of thermosolutal convection within a rectangular container has been investigated in this context by Cessi & Young (1992), Quon & Ghil (1992), and Thual & McWilliams (1992). These authors and others have discussed the problem's implications for long-term changes in the circulation of the Atlantic and world oceans. Quon & Ghil (1992, hereafter referred to as QG) showed that when symmetric restoring boundary conditions are applied on a horizontal boundary of the container, i.e. temperature T and salinity S are specified on the boundary, two convection cells symmetric about the central vertical axis of the container are the only steady solution. However, when the restoring boundary condition of a fixed salinity function is replaced instead by an appropriate salt-flux condition (i.e. a salinity gradient $\partial S/\partial z$ is imposed across the bottom boundary), the symmetric circulation may

transfer its stability to asymmetric circulations. We have established in QG that the bifurcated circulations can vary from arbitrarily slight asymmetry to a single-cell, antisymmetric state. Since the dominant cell can either be on the left or the right side of the container, the bifurcation is of the pitchfork type. Thual & McWilliams (1992) have reached independently similar conclusions. In this paper, we show that Hopf bifurcation may follow upon increasing the salt-flux strength further.

QG studied the Boussinesq equations for a non-dimensional parameter set $\Omega \equiv (Ra, \gamma, \lambda, \eta, \sigma, \delta)$, where Ra is the thermal Rayleigh number, γ the salt-flux strength, λ the salinity-to-temperature buoyancy ratio, η the Lewis number or the ratio of salt diffusivity to thermal diffusivity, σ the Prandtl number, and δ the container's aspect ratio. It was shown that the most important bifurcation parameters are the thermal Rayleigh number, Ra, and the salt-flux strength, γ. Consequently an approximate stability curve in the γ–Ra plane was constructed over 3 decades of Ra and over 2 orders of magnitude of γ (see figure 14 in QG). QG's results were all based on aspect ratios 0.2 and unity. The model is reviewed and small-δ scaling introduced in §§2 and 3.

We first investigate the limitations imposed by very small aspect ratio, δ, and the related effects of two additional parameters, $\mathscr{P}$ and $\mathscr{Q}$, on the circulation. The former is the ratio of the vertical to the horizontal viscosity coefficients, and the latter the corresponding ratio of diffusivities. Extremely small aspect ratios δ are studied for two specific reasons: (i) the aspect ratio of the oceans and most geophysical fluid systems is very small, and (ii) when δ is small, the departures of $\mathscr{P}$ and $\mathscr{Q}$ from unity become important. In §4, the boundary conditions on T and S imposed along the bottom of the box are monotonic, as they were in QG. They are both symmetric functions increasing with distance from the centre of the box towards both sidewalls.

In §§5 and 6, we investigate how non-monotonic, though still symmetric, boundary values of T and S affect the overall circulation. At the surface of the Atlantic Ocean, salt flux that is non-monotonic along a meridian is a prominent physical feature (Levitus 1982). We consider two types of non-monotonic conditions: (*a*) type A, for which both T and S are non-monotonic; and (*b*) type B, for which T is monotonic and S is non-monotonic, or vice versa. The non-monotonic T and S functions will be described later. At high Rayleigh number with $\delta \geqslant 0.2$, monotonic T and S restoring boundary conditions can produce non-monotonic salt fluxes (see QG), while at smaller δ, they produce essentially a monotonic salt flux with 'wiggles' at the end points. Non-monotonic restoring conditions produce non-monotonic salt fluxes even at very small δ. To ascertain that the salt flux is truly monotonic, we shall smooth out the aforementioned 'wiggles' of the salt flux when it is used as a boundary condition.

Concluding remarks follow in §7. The main conclusion is that our system can produce robust oscillations for the parameter range of interest. Hopf bifurcation appears to be an intrinsic property of thermosolutal convection with mixed boundary conditions. It is difficult, however, to relate in detail the oscillations in the present highly simplified model to those observed (Ghil & Vautard 1991; Allen, Read & Smith 1992*a*, *b*) or simulated (Mikolajewicz & Maier-Reimer 1990; Weaver, Sarachik & Marotzke 1991; Weaver *et al.* 1993; Chen & Ghil 1995) in the atmosphere and the oceans.

2. The model and scaling for small δ

A detailed description of the mathematical model and numerical methods is given in QG. We only present here some salient points that are relevant to the discussion of

rescaling The model consists of a rectangular box of arbitrary height-to-length aspect ratio, δ. The box contains a solute, e.g. salt. For the first stage of computation, the bottom of the box is maintained at prescribed temperature T and salinity S, that are functions of the horizontal coordinate. Such boundary conditions on both T and S are called 'restoring' in the recent oceanographic literature.

The sidewalls and the top boundary are thermally insulated and impermeable to salt. At the top of the box, a no-slip condition is imposed, while the rest of the boundaries are free-slip. All four boundaries are assumed rigid. Hence all normal velocities on the boundaries are set equal to zero, and total mass is conserved in the box. Along the bottom and the sidewalls, the tangential velocities are non-zero, but their normal gradients are required to vanish, i.e. these three walls support no tangential stress. Solutions for the problem with inhomogeneous boundary conditions imposed along the top are obtained from the present ones by reflection in a horizontal axis of symmetry.

After the system has attained a quasi-steady state, the salinity gradient across the bottom boundary is computed and used to replace the salinity function as the boundary condition there. The same temperatures are still prescribed on this boundary, leading to so-called 'mixed' boundary conditions for T and S. This stage of the computation may lead to symmetry breaking even for infinitesimal perturbations.

The governing equations are the two-dimensional Navier–Stokes equations and the heat- and salt-transport equations. As in QG, we shall introduce a Cartesian coordinate vector $\boldsymbol{X} = (x, z)$, and a velocity vector $\boldsymbol{V} = (u, w)$. However, we shall use different characteristic values to non-dimensionalize the equations: horizontal lengthscale L and vertical lengthscale H, L being the length and H the height of the box; velocity scales $U = (\kappa_{(h)T}\nu_{(h)})^{1/2}/H$ and $W = (\kappa_{(h)T}\nu_{(h)})^{1/2}/L$, $\kappa_{(h)T}$ and $\nu_{(h)}$ being respectively the horizontal components of the thermal diffusivity and kinematic viscosity tensors; timescale $\tau = L/U = H/W = LH/(\kappa_{(h)T}\nu_{(h)})^{1/2}$; and temperature and salinity scales ΔT and ΔS, being respectively the maximum temperature and salinity differences along the boundary of the enclosure.

The two-dimensional governing equations in non-dimensional form are

$$\partial u/\partial t + w\,\partial u/\partial x + u\,\partial u/\partial z = -\partial p/\partial x + (\sigma^{1/2}/\delta)(\delta^2\,\partial^2 u/\partial x^2 + \mathscr{P}\,\partial^2 u/\partial z^2), \tag{2.1}$$

$$\partial w/\partial t + u\,\partial w/\partial x + w\,\partial w/\partial z = -\delta^{-2}\,\partial p/\partial z + \delta Ra(T - \lambda S) + (\sigma^{1/2}/\delta)(\delta^2\,\partial^2 w/\partial x^2 + \mathscr{P}\,\partial^2 w/\partial z^2), \tag{2.2}$$

$$\partial T/\partial t + u\,\partial T/\partial x + w\,\partial T/\partial z = (\delta\sigma^{1/2})^{-1}(\delta^2\,\partial^2 T/\partial x^2 + \mathscr{Q}\,\partial^2 T/\partial z^2), \tag{2.3}$$

$$\partial S/\partial t + u\,\partial S/\partial x + w\,\partial S/\partial z = \eta(\delta\sigma^{1/2})^{-1}(\delta^2\,\partial^2 S/\partial x^2 + \mathscr{Q}\,\partial^2 S/\partial z^2), \tag{2.4}$$

$$\nabla \cdot \boldsymbol{V} = 0, \tag{2.5}$$

with the following boundary conditions:

$$\boldsymbol{V} = 0 \quad \text{at} \quad z = \delta, \tag{2.6a}$$

$$\partial u/\partial z = w = 0 \quad \text{at} \quad z = 0, \tag{2.6b}$$

$$u = \partial w/\partial x = 0 \quad \text{at} \quad x = 0, 1, \tag{2.6c}$$

$$\partial T/\partial n = \partial S/\partial n = 0 \quad \text{at} \quad z = \delta, x = 0, 1, \tag{2.6d}$$

where $\partial/\partial n$ denotes the normal gradients on the respective boundaries. The monotonic temperature and salinity boundary conditions are

$$T = T(x) = S(x) = 0.5(\cos 2\pi x - 1) \quad \text{at} \quad z = 0, \tag{2.6e}$$

or

$$T = T(x), \quad \partial S/\partial z = \gamma f(x) \quad \text{at} \quad z = 0; \tag{2.6f}$$

the non-monotonic conditions are defined below in (5.1). The equation of state is linear,

$$\rho = \rho_0(1 - \alpha T \Delta T + \beta S \Delta S); \tag{2.7}$$

here α and β are the coefficients of volumetric expansion for heat and salt respectively.

These equations are similar to those in QG, except for the explicit appearance of the aspect ratio $\delta = H/L$ in (2.1)–(2.4). The additional parameters $\mathscr{P}$ and $\mathscr{Q}$ are the ratios of the vertical-to-horizontal component of the viscosity and diffusivity, as defined in the next paragraph. Note that the same $\mathscr{Q}$ appears in both (2.3) and (2.4); we have thus tacitly assumed that the diffusivity ratios for heat and salt are equal. This is convenient, as well as justified by the fact that we do not really know what the difference between the two, if any, might be in the oceans.

The main non-dimensional parameters are δ,

the (thermal) Rayleigh number

$$Ra = \alpha g \Delta T L^3 / \kappa_{(h)T} \nu_h, \tag{2.8a}$$

the salt-to-heat buoyancy ratio

$$\lambda = \beta \Delta S / (\alpha \Delta T), \tag{2.8b}$$

the Lewis number

$$\eta = \kappa_{(h)S} / \kappa_{(h)T}, \tag{2.8c}$$

the Prandtl number

$$\sigma = \nu_{(h)} / \kappa_{(h)T}, \tag{2.8d}$$

the viscosity ratio

$$\mathscr{P} = \nu_{(v)} / \nu_{(h)}, \tag{2.8e}$$

and the diffusivity ratio

$$\mathscr{Q} = \kappa_{(v)T} / \kappa_{(h)T} = \kappa_{(v)S} / \kappa_{(h)S}, \tag{2.8f}$$

where ν and κ respectively stand for viscosity and thermal (or solute) diffusivity. Subscripts v and h denote the vertical and horizontal components of the corresponding (diagonal) tensors. This yields the following parameter set for the problem:

$$\Omega \equiv (Ra, \gamma, \lambda, \eta, \sigma, \delta, \mathscr{P}, \mathscr{Q}). \tag{2.9}$$

For water, $\sigma = O(10)$ and $\lambda = 0.32$.

The salinity gradient (salt flux) calculated from the symmetric quasi-steady state with boundary condition (2.6e) yields $f(x)$ in (2.6f), γ being the salinity flux strength, which is unity when the original flux is specified. However, we shall treat it as a free parameter. For almost all the computations in QG, $\gamma \leqslant 1.0$ was used. In this paper, $\gamma = 0.7$, 1.0, 1.5 and 3.0 will be used, while λ is fixed at 0.32. For $\gamma \approx O(1)$, changing $\partial S/\partial z$ by a factor γ on the boundary, cf. (2.6f), is essentially the same as changing S to γS throughout the domain, cf. (2.2)–(2.4) here and Appendix A in QG. Thus γ and λ are not independent parameters in the set Ω of (2.8), and QG showed that it is more practical to vary γ, while keeping λ fixed. Values of $\gamma\lambda < 1$ mean that we study temperature-dominated regimes, being motivated by the current circulation regime of the Atlantic Ocean (Bryan 1986; Chen & Ghil 1995).

Thus the parameter set Ω in QG is enlarged here to include $\mathscr{P}$ and $\mathscr{Q}$. In QG we have already investigated the effects that most of the parameters (2.9) have on the circulation, except those due to very small δ. The ratios $\mathscr{P}$ and $\mathscr{Q}$ were fixed at unity in QG and in other previous studies.

3. Approximations for small δ

When δ is small, the vertical diffusive terms can have dominant effects on both tracer and momentum transfers. Planetary flow systems usually have small aspect ratios and are dominated by advection. In this section, we show how $\mathscr{P}$ and $\mathscr{Q}$ affect the

boundary-layer thicknesses. In addition, we shall find an approximate solution for very small δ, and approximate threshold values of $\mathscr{P}$ and $\mathscr{Q}$ for which advection is the dominant tracer-transport mechanism at small δ.

3.1. *Boundary-layer scales*

Let us consider steady flows represented by the following linearized equations:

$$0 = -\partial p/\partial x + (\sigma^{1/2}/\delta)(\delta^2 \partial^2 u/\partial x^2 + \mathscr{P}\,\partial^2 u/\partial z^2), \tag{3.1}$$

$$0 = -\delta^{-2}\partial p/\partial z + \delta Ra\Lambda T + (\sigma^{1/2}/\delta)(\delta^2 \partial^2 w/\partial x^2 + \mathscr{P}\,\partial^2 w/\partial z^2), \tag{3.2}$$

$$u\,\partial \bar{T}/\partial x + w\,\partial \bar{T}/\partial z + \bar{u}\,\partial T/\partial x + \bar{w}\,\partial T/\partial z = (\delta\sigma^{1/2})^{-1}(\delta^2 \partial^2 T/\partial x^2 + \mathscr{Q}\,\partial^2 T/\partial z^2), \tag{3.3}$$

$$\nabla \cdot V = 0, \tag{3.4}$$

where the overbar denotes averaged values representative for the region of interest (e.g. the boundary layers). The T- and S-equations have been combined, with $(1-\lambda)$ replaced by Λ in (3.2), cf. QG. Neglecting the lower-order derivatives, we obtain the following vertical and bottom boundary-layer equations:

$$\partial^4 T/\partial x^4 = -(\Lambda \bar{T}_z\, Ra/\delta)\, T, \tag{3.5}$$

$$\partial^5 T/\partial z^5 = -\Lambda \bar{T}_x\, \delta^5 Ra(\mathscr{P}\mathscr{Q})^{-1}\,\partial T/\partial x. \tag{3.6}$$

It is clear from (3.5) that the vertical boundary-layer thickness is proportional to $Ra^{-1/4}$ and from (3.6) that the horizontal boundary-layer thickness is proportional to $Ra^{-1/5}$ (see Appendix B in QG). For small δ and small $\mathscr{P}$ and $\mathscr{Q}$, these layer thicknesses have the proportionality constants $\delta^{1/4}$ and $(\mathscr{P}\mathscr{Q})^{1/5}/\delta$, respectively. Thus if $\mathscr{P}\mathscr{Q}$ is large compared with δ, the bottom boundary layer is so thick that vertical diffusion dominates. On the other hand, if δ is kept constant and we assume that $\mathscr{P} = \mathscr{Q}$ are small, then the bottom-layer thickness will decrease roughly like $\mathscr{P}^{2/5}$. These proportionalities are not exact because other factors, such as $\bar{T}_x$ and $\bar{T}_z$, cannot be estimated *a priori*. But for sufficiently small $\mathscr{P}$ and $\mathscr{Q}$, the bottom boundary-layer thickness does decrease like the appropriate powers of $\mathscr{P}$ and $\mathscr{Q}$.

3.2. *Approximate solutions for infinitesimal* δ

How does very small δ affect overall circulation when $\mathscr{P}$ and $\mathscr{Q}$ are not small? In QG, pitchfork bifurcation occurred – for $\delta = O(1)$ and $\mathscr{P} = \mathscr{Q} = 1$ – due to a convective, nonlinear phenomenon, described heuristically by Walin (1985) and corresponding to large values of Ra. For δ small and $\mathscr{P} = \mathscr{Q} = 1$, Cessi & Young (1992) used an expansion in $\epsilon = \pi\delta$ to obtain analytic solutions dominated by diffusion. We show here how small δ inhibits advection for $\mathscr{P} = \mathscr{Q} = O(1)$.

For small δ, we can formally expand the dependent variables in series of ascending powers of δ:

$$u = \delta u^{(1)} + \delta^2 u^{(2)} + \ldots,$$

$$w = \delta w^{(1)} + \delta^2 w^{(2)} + \ldots,$$

$$p = p^{(0)} + \delta p^{(1)} + \delta^2 p^{(2)} + \ldots,$$

$$T = T^{(0)} + \delta T^{(1)} + \delta^2 T^{(2)} + \ldots,$$

$$S = S^{(0)} + \delta S^{(1)} + \delta^2 S^{(2)} + \ldots.$$

Substituting these power series into (2.1)–(2.5) and assuming steady state, we obtain the following equations, identical for the lowest two orders of each variable:

$$0 = -\partial p^{(0,1)}/\partial x + \sigma^{1/2}\mathscr{P}\,\partial^2 u^{(1,2)}/\partial z^2, \tag{3.7}$$

$$0 = -\partial p^{(0,1)}/\partial z + \delta^3 Ra(T^{(0,1)} - \lambda S^{(0,1)}), \tag{3.8}$$

$$0 = \partial^2 T^{(0,1)}/\partial z^2, \tag{3.9}$$

$$0 = \partial^2 S^{(0,1)}/\partial z^2, \tag{3.10}$$

$$\partial u^{(1,2)}/\partial x + \partial w^{(1,2)}/\partial z = 0. \tag{3.11}$$

These equations are based on the condition that $\mathscr{P} \gg \delta^2$ and $\mathscr{Q} \gg \delta^2$.

From (3.9) and (3.10) we see that, if $\mathscr{P}$ and $\mathscr{Q} \gg \delta^2$, vertical diffusion governs T- and S-transports. Equation (3.8) represents a hydrostatic balance. For the two terms in (3.8) to balance each other, we must have $Ra \sim \delta^{-3}$; for $\delta = 10^{-2}$, this would yield $Ra \sim 10^6$. This high value seems to contradict the rule of thumb that diffusive processes are expected to dominate transport only when Ra is small. Defining the Rayleigh number with H as the lengthscale – the way it is usually done for the Bénard problem, instead of L, as in (2.8a) – yields a new Rayleigh number, $Ra_H \equiv \delta^3 Ra$. Thus (3.8) would only require, formally, $Ra_H \sim O(1)$. However, (3.8) permits in fact a very wide range of values for Ra_H, as shown numerically in §4.1. In order to be consistent with QG, Ra is used throughout this paper, with the corresponding value of Ra_H only recalled, on occasion, for orientation purposes. Since we have kept $\delta = 0.01$ for all the numerical computations, $Ra_H = \delta^3 Ra = 10^{-6} Ra$ is easily calculated.

For illustration, we shall only solve the lowest-order equations (3.7)–(3.11), i.e. solve for u and w, accurate to $O(\delta^2)$ and p, T and S to $O(\delta)$. We shall integrate (3.8) directly to obtain the pressure as a function of T and S. Consider $\mathscr{P} = \mathscr{Q}$ to be $O(1)$, i.e. keeping the vertical and horizontal coefficients of viscosity and diffusivity equal in magnitude. From (3.9) and (3.10) the solution is

$$T^{(0)} = az + M(x),$$

where $M(x)$ is to be determined. To satisfy the boundary conditions (2.6d) and (2.6e), we require $a = 0$, and

$$T^{(0)} = M(x) = 0.5(\cos 2\pi x - 1); \tag{3.12}$$

$S^{(0)}$ has the same functional form as $T^{(0)}$ in (3.12) and is independent of z.

Since both solutions $T^{(0)}$ and $S^{(0)}$ have the same functional form, (3.8) can be written as

$$\partial p^{(0)}/\partial z = \Lambda_H T^{(0)},$$

where $\Lambda_H = Ra_H(1-\lambda)$. The solution $p^{(0)}$ is

$$p^{(0)} = \Lambda_H \int T^{(0)}\,dz = \tfrac{1}{2}\Lambda_H(\cos 2\pi x - 1)\,z + C(x), \tag{3.13}$$

where $C(x)$ is an arbitrary function of x, given by the boundary conditions. Since we do not know the boundary conditions for $p^{(0)}$, we shall determine $C(x)$ later.

From (3.7), the lowest-order balance for $u^{(1)}$ is

$$\partial p^{(0)}/\partial x = \mathscr{P}\sigma^{1/2}\,\partial^2 u^{(1)}/\partial z^2,$$

or

$$\partial^2 u^{(1)}/\partial z^2 = (\mathscr{P}\sigma^{1/2})^{-1}\,\Lambda_H\,\pi(-\sin 2\pi x)\,z + \partial C/\partial x.$$

After integrating the above equation once, we have

$$\partial u^{(1)}/\partial z = (\mathscr{P}\,\sigma^{1/2})^{-1}\,\Lambda_H\,\pi(-\sin 2\pi x)\,\tfrac{1}{2}z^2 + z\,\partial C/\partial x + D(x).$$

The boundary condition $\partial u/\partial z = 0$ at $z = 0$ gives $D(x) = 0$. Further integration yields

$$u^{(1)} = -\Lambda_H \pi z^3 (6\mathscr{P}\sigma^{1/2})^{-1} \sin 2\pi x + (\tfrac{1}{2}z^2)\,\partial C/\partial x + E(x). \tag{3.14}$$

Formally

$$w^{(1)} = -\int \partial u^{(1)}/\partial x \,\mathrm{d}z$$

$$= -\Lambda_H \pi^2 z^4 (12\mathscr{P}\sigma^{1/2})^{-1} \cos 2\pi x + \tfrac{1}{6}z^3\,\partial^2 C(x)/\partial x^2 + z\,\partial E(x)/\partial x + F(x). \tag{3.15}$$

Now we can apply the boundary conditions on $u^{(1)}$ and $w^{(1)}$ to determine $C(x)$, $E(x)$, and $F(x)$. Applying $u^{(1)} = 0$ at $z = \delta$ to (3.14) and $w^{(1)} = 0$ at $z = 0$ to (3.15) gives

$$E(x) = F(x) = 0; \tag{3.16}$$

(3.16) would also make $w^{(1)}$ satisfy the boundary condition at $z = \delta$, i.e. $w^{(1)} = 0 + O(\delta^3)$. At this stage one still cannot determine $\partial C(x)/\partial x$, because we have not included the $\partial^2 u^{(1)}/\partial x^2$ term in the lowest-order analysis. However, we can assume C to be an antisymmetric function like $\sin 2\pi x$, because u is antisymmetric, as later computations show. So basically the solutions are diffusion dominated at small δ. They consist of nearly vertical isotherms and isohalines, and the circulation contains two antisymmetric cells. It does not qualitatively differ from the low-Rayleigh-number flows at larger aspect ratios studied in QG.

The details of these conduction-dominated solutions have been studied analytically by Cessi & Young (1992). Here it suffices to conclude that, for $\mathscr{P} = \mathscr{Q} = O(1)$ at small δ, vertical diffusion dominates the momentum, as well as the heat and salt transport. As we shall show later, this statement holds even at very high Rayleigh number. Thus, to render advection dominant, as it is in geophysical flows, we must keep $\mathscr{P}$ and $\mathscr{Q}$ small. In the next section, we study therefore systematically the effects of decreasing $\mathscr{P}$ and $\mathscr{Q}$ on the circulation.

To help with the choice of parameters, let us examine the parameter values used in more highly resolved, three-dimensional ocean models, specifically those for the Atlantic Ocean. The north–south lengthscale of the Atlantic Ocean is approximately 10^4 km, and its representative depth is about 4 km. Hence the aspect ratio is $\delta = 4 \times 10^{-4}$. The following values of parameters are often used in oceanic general circulation models (OGCMs: Bryan & Cox 1968; Bryan 1986): the vertical eddy viscosity and eddy diffusivity are 1 $\mathrm{cm^2\,s^{-1}}$, and the horizontal eddy coefficients are $O(10^7)$ $\mathrm{cm^2\,s^{-1}}$. Hence $\mathscr{P}$ and $\mathscr{Q}$ are $O(10^{-7})$, on the same order of magnitude as $\delta^2 = 1.6 \times 10^{-7}$. The Rayleigh number based on lengthscale L and $\Delta T = 30$ °C, as defined in (2.8*a*), is about 3×10^{14}; Ra_H based on the ocean depth as a lengthscale is about 2×10^4. Thus, in OGCM experiments using these parameter values, the vertical and horizontal diffusion terms have the same order of magnitude. For such small values of δ, $\mathscr{P}$ and $\mathscr{Q}$, and high Rayleigh number, advection in both the momentum and the energy equations dominates diffusion as a transport mechanism.

These parameter values require, however, very high resolution throughout the domain, with even higher resolution in the boundary layers. Our main computations are limited to $\mathscr{P} = \mathscr{Q} = 0.01$, $\delta = 10^{-2}$, and $Ra_H \leqslant 10^6$ so as to permit a sufficiently broad exploration of parameter space and solution behaviour.

4. Monotonic boundary conditions for $Ra_H = 10^4, 10^5$

We consider first the restoring boundary conditions on T and S given in (2.6*e*), which are functions of x and symmetric about $x = 0.50$. As already pointed out, they increase monotonically with distance from the point of symmetry. The computational

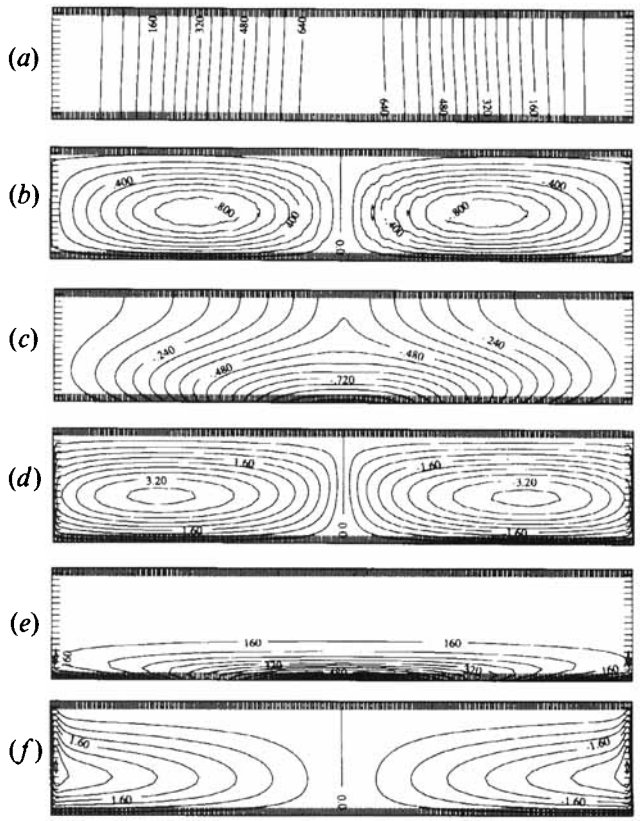

FIGURE 1. Symmetric states for monotonic boundary conditions and decreasing $\mathscr{P}$ and $\mathscr{Q}$ at $Ra = 10^{10}$. (*a*, *b*) $\mathscr{P} = \mathscr{Q} = 1.0$: (*a*) isotherms T = const., $T_{min} = 1.00$, $\Delta T = 0.06$ for this and all subsequent T-plots; (*b*) streamlines ψ = const., $\psi_{max} = 0.72$, $\Delta\psi = 0.09$. (*c*, *d*) $\mathscr{P} = \mathscr{Q} = 0.10$: (*c*) isotherms; (*d*) streamlines, $\psi_{max} = 3.20$, $\Delta\psi = 0.40$. (*e*, *f*) $\mathscr{P} = \mathscr{Q} = 0.01$: (*e*) T-field; (*f*) ψ-field, $\psi_{max} = 3.60$, $\Delta\psi = 0.45$. Vertical scale exaggerated by a factor of 20, in this and all subsequent plots.

mesh used in the present section consists of 300×20 equally spaced grid points. All computations for $Ra > 10^{11}$, as well as those for non-monotonic boundary conditions at all Ra-values (§§5 and 6), deploy meshes consisting of 300×30 grid points. In §4.1, it suffices to consider restoring boundary conditions, while mixed boundary conditions are used in §§4.2, 5 and 6.

4.1. *Symmetric solutions at decreasing values of $\mathscr{P}$ and $\mathscr{Q}$, $Ra_H = 10^4$*

In §3.2 we saw that flows are diffusion dominated when δ is sufficiently small, and $\mathscr{P}$ and $\mathscr{Q}$ are of order unity. As $\mathscr{P}$ and $\mathscr{Q}$ are reduced, the influence of diffusion on both the momentum and energy equations will decrease. How transport mechanisms compete and advection gains dominance is illustrated in this section. As in QG, we use $\sigma = 2.25$ and $\eta = 1$ throughout (see §4.2.2(iv) of QG for different values of σ and η).

Figure 1 (*a–f*) shows the isotherms and the stream-function contours for three sets of decreasing values of $\mathscr{P}$ and $\mathscr{Q}$: $\mathscr{P} = \mathscr{Q} = 1.00$, 0.10, and 0.01, at $\delta = 0.01$. As explained in QG, the salinity distribution is exactly the same as the temperature distribution for restoring boundary conditions and $\eta = 1$. From (2.1)–(2.4), we see that $\mathscr{P}$ and $\mathscr{Q}$ must be of order $\delta^2 (= 10^{-4})$ for the horizontal and vertical diffusion terms in both the momentum and energy equations to have equal strength. As shown in §3.1, the

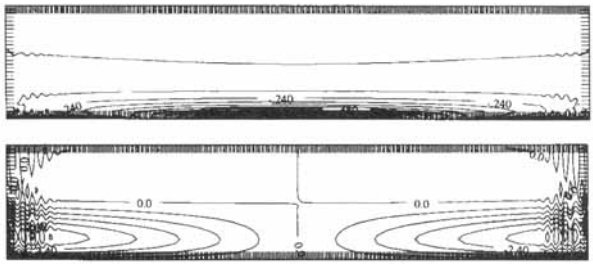

FIGURE 2. Symmetric states for restoring boundary conditions, $\mathscr{P} = \mathscr{Q} = 0.01$, and $Ra = 10^{11}$. (*a*) Isotherms; (*b*) streamlines, $\psi_{max} = 4.80$, $\Delta\psi = 0.60$.

thickness of the horizontal boundary layer is proportional to $(\mathscr{P}^2/Ra)^{1/5}$: many more grid points in the vertical would be needed to resolve reasonably well the equations at $\mathscr{P} = 10^{-4}$. We have not carried out a computation for $\mathscr{P}$ smaller than 0.01, since these three cases are adequate for illustrative purposes. We focus on whether the system is advection dominated for a given Ra, $\mathscr{P}$ and $\mathscr{Q}$, rather than on the comparative importance of vertical and horizontal diffusion.

Figures 1(*a*)–1(*f*) are exaggerated by a factor of 20 in the z-direction. Figure 1(*a*) shows that the isotherms (and, implicitly, isohalines) are almost vertical. Hence even at $Ra = 10^{10}$ (or $Ra_H = 10^4$), the tracer transports are governed by vertical diffusion when $\mathscr{P}$ and $\mathscr{Q}$ are of order unity, as predicted in the last section. In fact, this still holds for $Ra = 10^{11}$ (not shown). The circulation in figure 1(*b*) consists of two symmetric cells.

As $\mathscr{P}$ and $\mathscr{Q}$ decrease from unity to 0.10, the dominance of vertical diffusion over horizontal diffusion has clearly diminished, as seen from the isotherms shown in figure 1(*c*) no longer being vertical. For this set of parameters, both the distribution of isotherms and the circulation (figure 1*d*) are very similar to low-Ra flows studied in QG at $\delta = O(1)$.

As $\mathscr{P}$ and $\mathscr{Q}$ are further reduced from 0.10 to 0.01, the streamlines show substantial flow reversal in the sidewall boundary layers (figure 1*f*). The interior isotherms have been extensively compressed by downward flows (figure 1*e*), and the fluid has become strongly stratified in the vertical. Obviously advective transport has become more important in the interior. The maxima of the two cells have migrated towards the sidewalls, implying much stronger boundary-layer flows along the vertical boundaries. The horizontal boundary layer is also much better defined (see figure 1*f*).

These computations show that one must have $\mathscr{P} \ll 1$ and $\mathscr{Q} \ll 1$ to induce an advection-dominated state for small δ. If we use $\mathscr{P} = \mathscr{Q} = 1$, no such state can be attained at any reasonable Ra-value.

4.2. *Asymmetric steady states at* $Ra_H = 10^5$, $\gamma = 1.5$

We concentrate in this subsection on $Ra = 10^{11}$, although some of the phenomena studied below also exist at lower values of Ra. When increasing Ra by a factor of 10, from 10^{10} to 10^{11}, the symmetric state changes greatly. Figures 2(*a*) and 2(*b*) show the temperature and stream function at $Ra = 10^{11}$. By comparing them with figures 1(*e*) and 1(*f*), which are their counterparts at $Ra = 10^{10}$, three features stand out very prominently. First, figure 2(*a*) shows that increasing Ra by a factor of 10 reduces the bottom thermal layer thickness by about half. Comparing the two temperature profiles (not shown here) yields a good estimate for the ratio of the boundary-layer thicknesses in the two cases, $(Ra_1/Ra_2)^{1/5} = 10^{-1/5} \approx 0.63$, as discussed in §3.1. A second

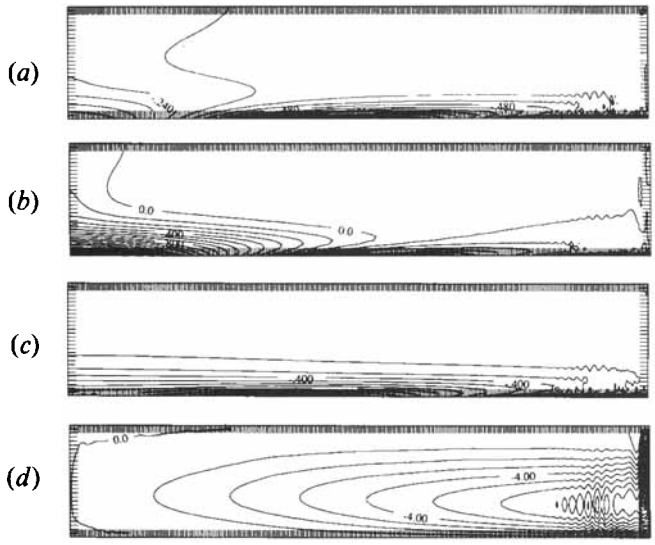

FIGURE 3. Asymmetric state for monotonic boundary conditions at $Ra = 10^{11}$, $\mathscr{P} = \mathscr{Q} = 0.01$, and $\gamma = 1.5$. (*a*) Temperature; (*b*) salinity, $S_{min} = -0.70$, $S_{max} = 1.90$, $\Delta S = 0.10$; (*c*) density anomaly, $\rho_{min} = -0.80$, $\rho_{max} = 0$, $\Delta\rho = 0.05$; and (*d*) stream function, $\psi_{min} = -16.0$, $\psi_{max} = 0$, $\Delta\psi = 1.00$.

prominent feature is the small-scale oscillations near the sidewalls (figure 2*b*). These spatial oscillations result from the unstable density gradient set up by strong horizontal advection of isopycnals in these areas; recall that the salinity, and hence density, plots are identical to that of the temperature in figure 2(*a*). This small-scale cellular convection is probably related to Rayleigh–Bénard instability; its horizontal and vertical scales are comparable and well resolved numerically.

A third feature is that, away from the sidewalls, the streamlines are confined to the container's bottom half. This confinement is partly because the boundary-layer thickness has been reduced by a factor of 0.63 as pointed out above, and partly for the following physical reason. Figure 1(*f*) shows that for $Ra = 10^{10}$, the sidewall layer carries the fluid from the bottom to the top. Detrainment from the boundary layer takes place in the top half of the container. It appears that the oscillations shown in figure 2(*b*) have drained the energy of the fluid locally and prevent it from rising higher. Consequently, the upper half of the fluid remains relatively undisturbed.

A mathematical explanation is that boundary layer solutions often have an oscillatory component in addition to the exponentially decaying one. Since the horizontal boundary layer is so much thinner for $Ra = 10^{11}$, there is room in the vertical to accommodate the first zero crossing of this oscillatory component and hence a counter cell. The stream function maximum has increased from 3.2 to 4.8, an increase of 50%, when Ra is increased from 10^{10} to 10^{11}. The spatial oscillations are very localized, and the interior streamlines remain quite smooth. The overall features show that, as expected, the flow and tracer transports become much more nonlinear at $Ra = 10^{11}$ than at $Ra = 10^{10}$.

By analogy with the higher-δ situation in QG at $\mathscr{P} = \mathscr{Q} = 1$, we expect a pitchfork bifurcation from the symmetric states of figures 1 and 2, where $\gamma = 1$, to states with an increasing loss of symmetry as γ increases. A highly supercritical state exhibiting a one-cell circulation is shown in figure 3, for $\gamma = 1.5$. Figures 3(*a*)–3(*d*) give the temperature T, the salinity S, the density anomaly $\rho = T - \lambda S$, and the stream function ψ. We have included ρ to show how delicately and precisely the temperature and salinity balance

each other to maintain a stable density structure within the fluid. The isotherms in figure 3(*a*) and the isohalines in figure 3(*b*) have, in this highly asymmetric flow, very different structures. One would expect that either T or S could independently generate some strong cells on the left side of the box, because of their strong horizontal gradient in that region. However, the combined effects are very different (figure 3*c*): the isopycnals are almost horizontal everywhere in the fluid's interior, very much like those in the oceans. The wiggles in the isopycnals on the right side correspond to the spatial oscillations of the flow, as shown in figure 3(*d*).

This one-cell state resembles well in its major features those studied by QG for higher aspect ratios and smaller Ra. The main difference here is provided by the spatial oscillations, which did not exist in the previous cases. The dimensionless stream-function maximum is 16.0, about 3 times larger than that for $Ra = 10^{10}$ and $\gamma = 1.0$, which is 5.1 (see figure 5*a* below). A very strong and slender vertical cell exists at the right sidewall and is part of the vertical boundary layer. The flows in the interior of the fluid are relatively weak and laminar. If there is a second bifurcation, it is likely to originate in an instability localized near the right sidewall.

In §6.2, we explore the γ–Ra parameter space at higher γ, i.e. using larger salt flux on the horizontal boundary. In QG, we did show at lower Rayleigh number, $Ra \leqslant 10^5$, that $\gamma \geqslant 1.0$ can produce asymmetric flows which would otherwise be symmetric at lower values of γ. However, the domain $\gamma > 1.0$ was not explored in QG at higher Rayleigh numbers, $Ra \geqslant 10^6$ (see figure 14 there).

In general, as the stress on a fluid system increases, one expects successive bifurcations to lead to more and more complex flows, until (weak) turbulence is reached. A number of such scenarios in geophysical fluid dynamics are reviewed by Ghil & Childress (1987) and Ghil, Benzi & Parisi (1985). Based on the simplified OGCM results of Mikolajewicz & Maier-Reimer (1990) and of Weaver *et al.* (1991), one would expect the next bifurcation in this system to be a Hopf bifurcation to oscillatory solutions. We have indeed found such bifurcations for both monotonic and non-monotonic boundary conditions. Hopf bifurcation is studied in detail in §5.3 below; the results for monotonic boundary conditions (not shown) are quite similar. The independence of the oscillatory solutions from a specific form of boundary conditions is discussed in §7.

5. Type-A boundary conditions, $Ra_H = 10^4$–10^6

To study Hopf bifurcation in the presence of non-monotonic salt flux, we compute first steady flows due to non-monotonic restoring conditions. As shown in the Appendix, these conditions produce non-monotonic salt fluxes, which are then imposed on the boundary and can give rise to oscillatory solutions. To explore Ra-values appropriate for the ocean, it is desirable to explore the flows at the highest Ra attainable by our computational resources. We thus conduct investigations up to $Ra = 10^{12}$ ($\delta^3 Ra = 10^6$).

To be consistent with §4, we have confined our studies exclusively to $\mathscr{P} = \mathscr{Q} = 0.01$. The monotonic T- and S-functions in (2.6*e*), used for all computations carried out in QG and in this study so far, are now changed to the non-monotonic function

$$T = T(x) = S(x) = \tfrac{1}{2}(\sin 3\pi x - 1) \quad \text{at} \quad z = 0; \tag{5.1}$$

T and S are still symmetric about $x = \frac{1}{2}$, where they reach a minimum value of -1. They increase in magnitude with distance away from $x = \frac{1}{2}$, reaching maximum values of zero at $x = \frac{1}{6}$ and $\frac{5}{6}$. Then they decrease again towards $x = 0$ and 1. We have chosen

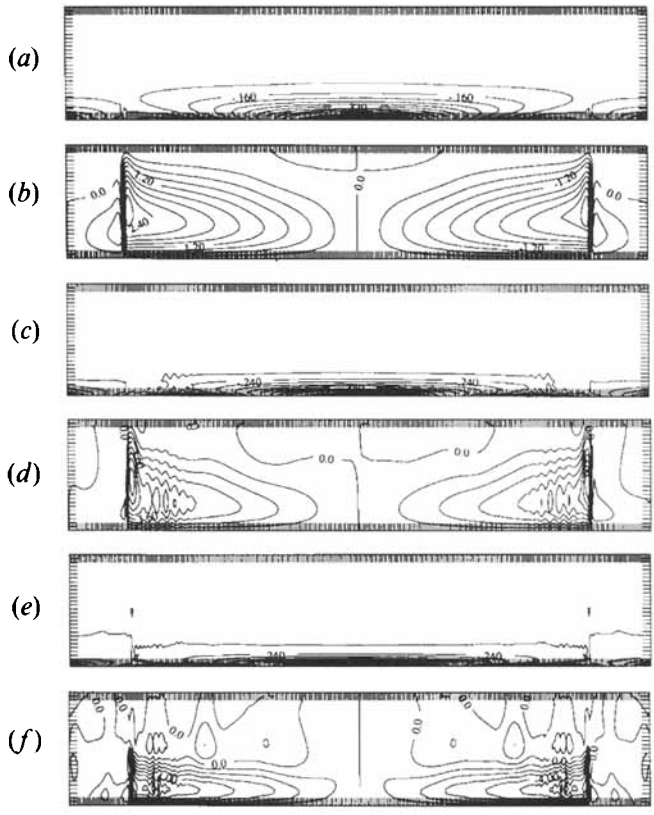

FIGURE 4. Symmetric steady states for type-A restoring boundary conditions at $\mathscr{P} = \mathscr{Q} = 0.01$ and $Ra = 10^{10}$, 10^{11} and 10^{12}. (*a*, *b*) $Ra = 10^{10}$: (*a*) T, (*b*) ψ, $\psi_{max} = 2.70$, $\Delta\psi = 0.30$; (*c*, *d*) $Ra = 10^{11}$: (*c*) T, (*d*) ψ, $\psi_{max} = 7.20$, $\Delta\psi = 0.90$; (*e*, *f*) $Ra = 10^{12}$: (*e*) T, (*f*) ψ, $\psi_{max} = 10.0$, $\Delta\psi = 1.00$.

these boundary profiles for T and S because they will create a non-monotonic salt flux. To ensure that the flows are convection dominated, we investigate the circulation at three different Rayleigh numbers: $Ra = 10^{10}$, 10^{11}, and 10^{12}. The corresponding time-step sizes are $\Delta t = 1 \times 10^{-7}$, 5×10^{-8}, and 2×10^{-8}, respectively, to ensure computational stability.

5.1. *Symmetric solutions*

The symmetric states obtained at $Ra = 10^{10}$ with restoring boundary conditions (5.1) are discussed first. Figures 4(*a*) and 4(*b*) are respectively the near steady-state temperature and stream function in this case. Comparing these with figures 1(*e*) and 1(*f*) in §4.1 shows the difference in response to the non-monotonic boundary conditions at the same Ra. These differences are most obvious in figure 4(*b*), namely, the two internal boundary layers, or plumes. They are situated at some distance from the side boundaries because the temperature maxima are at $x = \frac{1}{6}$ and $\frac{5}{6}$, instead of 0 and 1 as in QG and §4 here. These plumes are not situated, however, at the temperature maxima, but at a distance approximately $\frac{1}{12}$ from the walls (recall that the total width is unity). The shift in the plumes' positions indicates strong horizontal advection within the bottom boundary layer towards the walls.

The plume proper is very narrowly confined within two or three grid points. This shows that – even with 300 grid points in the horizontal direction – the numerical resolution is barely adequate to represent this particular part of the flow field. It is not possible to stretch coordinates to resolve the plumes, as is done for the boundary layers

(see (3.6*a*, *b*) in QG), because we do not know beforehand the location of the plumes. The problem is even more complicated when moving internal fronts are present, as in the (weakly) oscillatory solutions shown in §5.3 below. But the temperature and salinity fields are reasonably well resolved in the horizontal boundary layer. For the bulk of the fluid in the upper half of the container, T and S are almost uniform. The similarities between the symmetric steady states induced by monotonic and by type-A boundary conditions are more striking than their differences. The portions of the mass and velocity fields between the two plumes in figures 4(*a*) and 4(*b*) resemble figures 1(*e*) and 1(*f*) quite well.

Figure 4(*c–f*) depicts temperature fields and stream functions for the two higher Rayleigh numbers, $Ra = 10^{11}$ and 10^{12}. The stream function plots in figures 4(*b*), 4(*d*) and 4(*f*) all consist of two main cells. For all three *Ra*-values, the internal layers are situated approximately at the same x-positions. A number of differences, though, are evident. The plumes' depth penetration for the two lower *Ra*-values is quite similar but the plumes stop at mid-depth for $Ra = 10^{12}$ (figure 4*f*). The streamlines for $Ra = 10^{10}$ in figure 4(*b*) are very smooth, with no sign of standing waves. On the other hand, figure 4(*d*) shows a great deal of short-wave structure, indicating that waves born of the vertical plumes are propagating towards the interior at almost all depths, while no sign of internal oscillation exists between the plumes and the sidewalls. The main cells only occupy the lower half of the enclosure, but there are additional, weaker cells in the upper part of the fluid. This case, unlike the one for $Ra = 10^{10}$, never reached a true equilibrium. In figure 4(*f*) two weak fronts are travelling inward toward the centre of the container, but get weaker as they progress. After they have dissipated, new fronts are formed. These processes take place very slowly.

Quantitatively, the absolute stream function maximum increases from 2.70 to 7.20 and then to 10.0 as the Rayleigh number increases from 10^{10} through 10^{11} to 10^{12}. The horizontal velocity maxima increase from 1300 to 4500 and then to 9000. The vertical velocity maxima increase from 510 to 1800 and then to 3200, all in non-dimensional units (not shown). Roughly speaking, an increase by a factor of 10 in *Ra* produces a flow two or three times as vigorous. The overall effects of higher Rayleigh numbers on the flows are generally expected, although the complexity of the flows at the higher *Ra*-values cannot be anticipated. The horizontal boundary-layer thicknesses indeed decrease in proportion to $Ra^{-1/5}$: an order of magnitude increase in *Ra* reduces the boundary-layer thickness by a factor of 0.63. This reduction can be roughly estimated from the three isotherm structures in figures 4(*a*), 4(*c*) and 4(*e*).

5.2. *Asymmetric steady states at* $\gamma = 1.0$

We first show the differences between the asymmetric steady states obtained when using mixed boundary conditions, monotonic or of type A. Figures 5(*a*) and 5(*b*) show the stream function when $Ra = 10^{10}$ and the boundary condition used is of one or the other type. It is clear that non-monotonicity has produced but small quantitative changes in the results: the absolute maximum is 5.1 in the former *vs.* 4.8 in the latter. However, the internal boundary layer of the latter is very clearly detached from the sidewall, as are those in the symmetric flow (figure 4*b*, *d*, *e*). The plume here has shifted even further away from the temperature maximum, towards the sidewall. A very small secondary cell occurs between the boundary layer and the sidewall. Most conspicuous in the stream function of figure 5(*b*) is the substantial increase of wave-like structure compared with that in figure 5(*a*). These small-scale structures extend slightly beyond the temperature maximum on the horizontal boundary, i.e. throughout the area that is gravitationally most unstable.

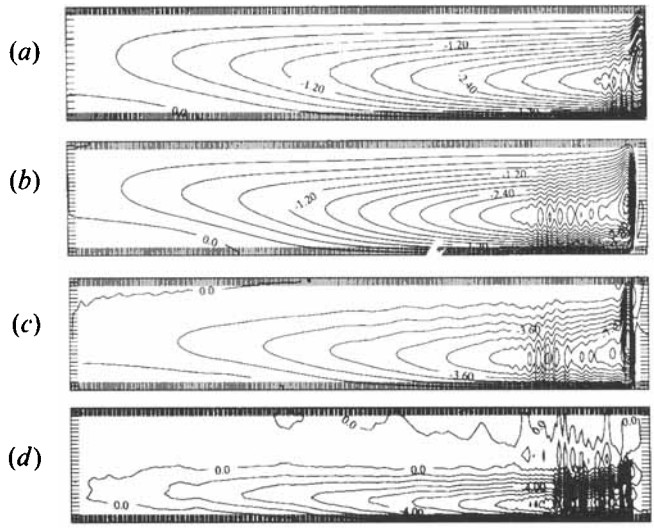

FIGURE 5. Asymmetric stream-function fields at $\gamma = 1.0$, for monotonic (a) and type-A (b–d) boundary conditions. (a) $Ra = 10^{10}$, monotonic, $\psi_{min} = -5.10$, $\psi_{max} = 0$, $\Delta\psi = 0.30$; (b) $Ra = 10^{10}$, type A, $\psi_{min} = -4.80$, $\psi_{max} = 0$, $\Delta\psi = 0.30$; (c) $Ra = 10^{11}$, $\psi_{min} = -12.0$, $\psi_{max} = 0.80$, $\Delta\psi = 0.80$; and (d) $Ra = 10^{12}$, $\psi_{min} = -13.50$, $\psi_{max} = 0.90$, $\Delta\psi = 0.90$.

The asymmetric solutions for the type-A boundary condition at higher Ra do not differ very substantially from that at $Ra = 10^{10}$ discussed above. All are essentially one-cell asymmetric circulations, as shown in figures 5(c) and 5(d), for $Ra = 10^{11}$ and 10^{12}. As the Rayleigh number increases, the internal spatial oscillations become ever more vigorous, although comparing figures 5(b), 5(c), and 5(d) shows that their horizontal extent changes but little at different Ra. The cell shapes are very similar in figures 5(b) and 5(c), while the cell height decreases in figure 5(d). However, the cell strengths do differ: the absolute stream function maximum is 4.8 in figure 5(b), about 12.0 in figure 5(c), and 13.5 in figure 5(d). The latter plot also shows a more complex flow pattern. The internal oscillations are much more vigorous than those for the lower Ra. Thus, the asymmetric states for all three Ra-values are quasi-steady one-cell circulations at $\gamma = 1.0$. Large-scale oscillations, if any, will presumably arise at higher values of γ.

5.3. *Oscillatory solutions at* $\gamma = 1.5$

As shown in figure 12(a) in the Appendix, the salt flux for a monotonic restoring condition at small δ is essentially monotonic. It strongly differs from those shown in QG for larger values of δ, which are non-monotonic even when the restoring conditions are monotonic. Figures 12(b) and 12(c) show that, at small δ, the salt fluxes for non-monotonic restoring conditions are also non-monotonic.

The total kinetic energy for an oscillatory solution at $Ra = 10^{11}$ and $\gamma = 1.5$, using mixed boundary conditions based on the salt flux from a type-A restoring condition, is plotted in figure 6. This particular computation was run for nearly a million time steps. Computations for the symmetric states of high-Rayleigh-number flows in §5.1 were started with a lower Ra. After the changes in the flow regime start to equilibrate, the Rayleigh number is increased. Each increase in Ra-value may require a reduction in Δt. This procedure brings the computation gradually to the desired region in parameter space. The computation discussed in this section started with $Ra = 10^{10}$, but after 10^5 time steps, the Rayleigh number was raised to 10^{11}.

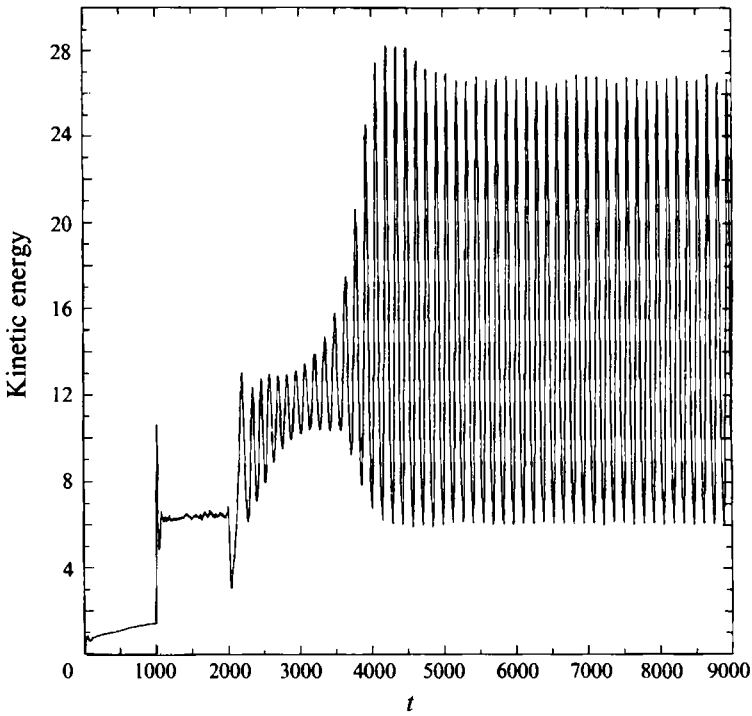

FIGURE 6. The time evolution of kinetic energy for type-A boundary conditions at $Ra = 10^{11}$, $\gamma = 1.5$ and $\mathscr{P} = \mathscr{Q} = 0.01$. Time on the abscissa in multiples of 100 time steps.

As figure 6 shows, the system has reached a quasi-equilibrium state at time step 2×10^5. Then the restoring boundary condition for salinity is replaced by the salt-flux condition and a very small perturbation, $O(10^{-3})$, is introduced next to the bottom in the container's right half at the next time step. As a result, the kinetic energy increases in the mean and starts to oscillate with a period of about 14 k (1 k = 1000 time steps).

The initial overshoot that occurs at 200 k decays and the oscillations slowly decrease in amplitude up to 300 k. Then the amplitude increases again exponentially and reaches its maximum near time step 420 k, while the period stays near 14 k. The amplitude of the oscillation decreases somewhat till 500 k and is modulated with a longer period, equal to 7 or 8 periods of the basic oscillation. The modulating amplitude is very small, but shows the possibility of an additional oscillatory mode which may be more prominent at larger γ. There is no doubt that the large-amplitude, rather regular oscillations sustained between 500 k and 900 k are a major feature of the system. Now the interesting questions to answer are the following: What is the nature of these oscillations and what is the dynamics governing them? We shall try to answer these questions next.

Between 200 k, when the perturbation is applied, and up to 400 k time steps, figure 6 indicates that the velocity field develops intensely, with an explosive growth of kinetic energy. During this time interval, the flows consist of a single cell (not shown here) whose strong core remains stationary. The cell is detached from the sidewall. A number of small-scale oscillatory features can be interpreted as internal waves, as in figure 5. Figure 6 shows that, at time step 320 k, the normalized mean energy is about 11 and the amplitude of the oscillations about 1.0. During this time interval, the single cell preserves its shape fairly well, but the absolute stream-function maximum oscillates

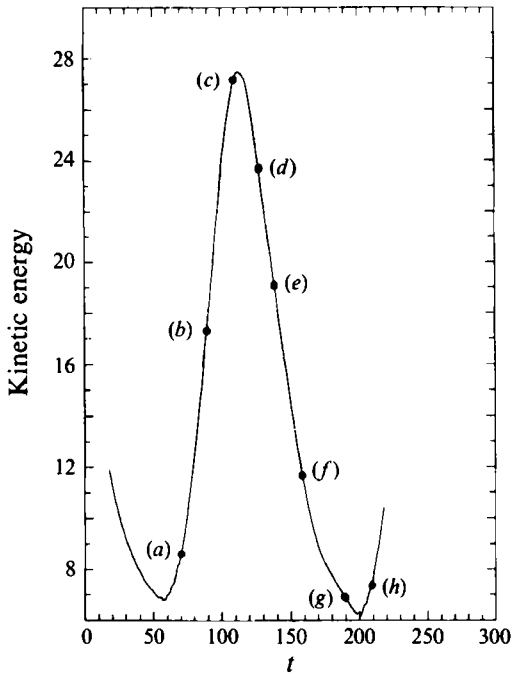

FIGURE 7. Enlarged portion of the kinetic energy evolution in figure 6. The solid circles correspond to the consecutive stream-function plots in figure 8(*a–h*).

from 12.8 to 9.6. Therefore, the oscillation manifests itself as a periodic change in the strength of the single cell.

The system equilibrates to a steady large-amplitude oscillation from time step 500 k onward. During the equilibration, the mean kinetic energy is about 16 and the amplitude of the oscillation is 10.5, ten times larger than before. The most remarkable feature of figure 6 is the regularity of these oscillations both in amplitude and frequency.

Figure 7 shows an enlarged cycle of the kinetic energy, and in figure 8(*a–h*) we show a selected number of plots of the stream function over the period of one oscillation (see solid circles in figure 7). Most interesting is the number of cells that appear and disappear during the cycle. The number changes from one when the kinetic energy is maximum (figure 8*c*) to four at low kinetic energy (figure 8*g*). Kagan & Maslova (1990) are the only previous authors studying related problems to have reported on multiple-cell formation. These authors were working on a three-layer ocean model and showed schematic diagrams of a varying number of cells. The change in the number of large-scale cells here, along with the small-scale features near the plume (figure 8*d–g*) and the propagation of a front from the plume into the more quiescent part of the flow (figure 8*b–f*), suggest that the dynamics of these oscillations is rather complex and requires further study.

Figure 8(*a–h*) covers a complete cycle of the oscillation. Near minimum energy (figure 8*g*), the circulation consists of four cells in the fluid's locally stable part, i.e. that portion of fluid on the left side of the enclosure not containing the persistent internal waves on the right. The largest and strongest cell, in the lower-right side of the container, has a gravitationally unstable region where strong small-scale internal oscillations occur. These internal waves are well resolved by our grid, with about 12 grid points per wavelength. Shortly past the energy minimum (figure 8*a*, *h*), the minor

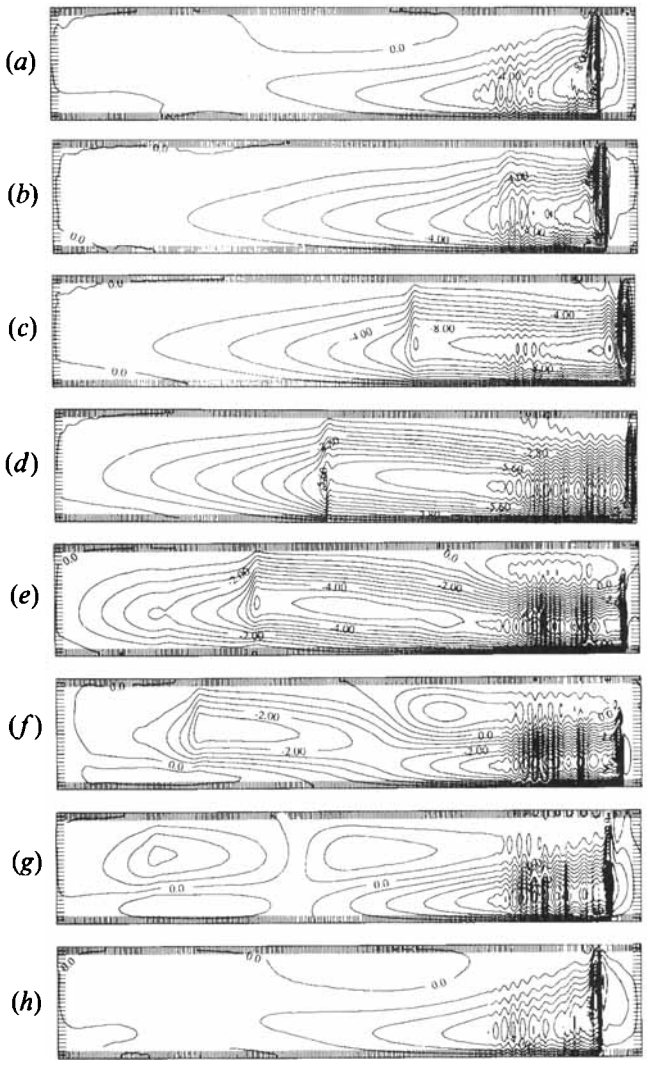

FIGURE 8. Stream-function plots at regular intervals during a complete oscillation cycle for $Ra = 10^{11}$ and $\gamma = 1.5$: (*a*) 402 k, $\psi_{min} = -13.00$, $\psi_{max} = 3.00$, $\Delta\psi = 1.00$; (*b*) 404 k, $\psi_{min} = -17.00$, $\psi_{max} = 1.00$, $\Delta\psi = 1.00$; (*c*) 406 k, $\psi_{min} = -17.00$, $\psi_{max} = 1.00$, $\Delta\psi = 1.00$; (*d*) 408 k, $\psi_{min} = -10.50$, $\psi_{max} = 0.70$, $\Delta\psi = 0.70$; (*e*) 410 k, $\psi_{min} = -7.00$, $\psi_{max} = 1.50$, $\Delta\psi = 0.50$; (*f*) 412 k, $\psi_{min} = -6.50$, $\psi_{max} = 1.50$, $\Delta\psi = 0.50$; (*g*) 414 k, $\psi_{min} = -7.20$, $\psi_{max} = 2.40$, $\Delta\psi = 0.60$; and (*h*) 416 k, $\psi_{min} = -12.0$, $\psi_{max} = 4.00$, $\Delta\psi = 1.00$.

cells disappear, and the main cell shrinks to minimum size. The strong internal boundary layer is positioned further to the left of the right boundary than at any other time during the cycle. Between the plume and the vertical wall, there is a weak but visible counter cell. The vertical plume is so strong that only part of it is detrained into the interior, while the rest falls back down directly to form a very slender cell with the original plume. Tremendous shear occurs, therefore, in this region.

To the left of this slender cell and separated from it by a region of relatively smooth flow is a strong internal wave packet, situated exactly at the location of the temperature maximum. While the kinetic energy is on the upswing (figure 8*a*), this packet of internal waves has become so strong that its envelope builds up to a front, similar to

a solitary wave or an internal bore (figure 8*b*). There is some resemblance, possibly fortuitous, to internal solitary waves generated by abrupt topography in the ocean (Quon & Sandstrom 1990; Sandstrom & Quon 1994) and to convective microstructures observed on smaller scales (Gregg 1987). The front remains vertical as it propagates to the left (figure 8*c–e*). There is also simultaneous displacement of the plume towards the right wall (figure 8*a–d*) and a growth of slender convective cells between the boundary maximum of the temperature and the plume (figure 8*b–e*). The kinetic energy of the system reaches its maximum just after figure 8(*c*), and will then decline very rapidly.

The integrated heat flux across the bottom boundary (not shown) evolves roughly in quadrature with the kinetic energy. The system absorbs heat when the kinetic energy increases, does not exchange heat with the exterior when the energy is at an extremum, and the heat is drained out of the system when the energy decreases. The internal dynamics redistributes the temperature near the bottom boundary and in the interior, thus helping sustain the oscillation.

In figure 8(*d*), the front has advanced past the mid-point of the container, and has steepened further. Note also that the front is much steeper near the bottom where it is advancing against the main circulation; within the top half it is less steep because it is advancing with the large-scale flow. In the same panel, reflection of the right-most penetrating slender convection cell from the right sidewall is apparent, helping form the internal waves shown here. As this slender cell is carried leftward, away from the wall, a number of additional cells – which do not extend through the entire depth of the fluid – are formed and compressed between the penetrating cell and the boundary maximum of the temperature (figure 8*d–g*). In figure 8(*e*), the front has dissipated considerably, especially in the container's bottom half where the fluid is strongly stratified. On the right, two secondary cells, one near the upper-right corner, and another underneath it, have begun to form. In figure 8(*f*), when the kinetic energy is approaching its minimum, the front on the left has almost disappeared. The two cells on the right have strengthened, and a fourth cell at the lower left corner is starting to appear. Finally in figure 8(*g*), when the kinetic energy has almost reached its lowest level, four cells are quite prominent, after which the cycle repeats itself. Note that throughout the whole cycle, the slender cell formed by the internal boundary layer never loses its identity. It is carried back and forth by the gravitationally unstable region, where the rising plume supplies the energy.

The evolution of kinetic energy and of the flow patterns for monotonic boundary conditions (not shown) is quite similar. The only two major differences are that: (i) the mean kinetic energy and its amplitude in the sustained oscillatory regime are both smaller; and (ii) no detached plume occurs, strongest horizontal gradients being confined to the neighbourhood of the right wall. Internal wave packets and multiple cells do still occur, although they are weaker than for the A-type boundary conditions studied here in detail.

How prevalent are oscillatory solutions in the system under investigation? For example, at the aspect ratio we have fixed here, does Hopf bifurcation occur at higher or lower Rayleigh numbers than 10^{11}? Furthermore, where would periodic solutions cease to exist if we decrease γ from its present value of 1.5? Does Hopf bifurcation occur for the higher aspect ratios studied in QG? If so, at what values of γ? These general questions can only be answered by constructing a hypersurface in parameter space consisting of Hopf bifurcation points. It is numerically too demanding – given the number of parameters – to do so and answer all these questions, but we show here for illustration purposes a Hopf bifurcation diagram for $Ra = 10^{11}$ with type-A boundary conditions.

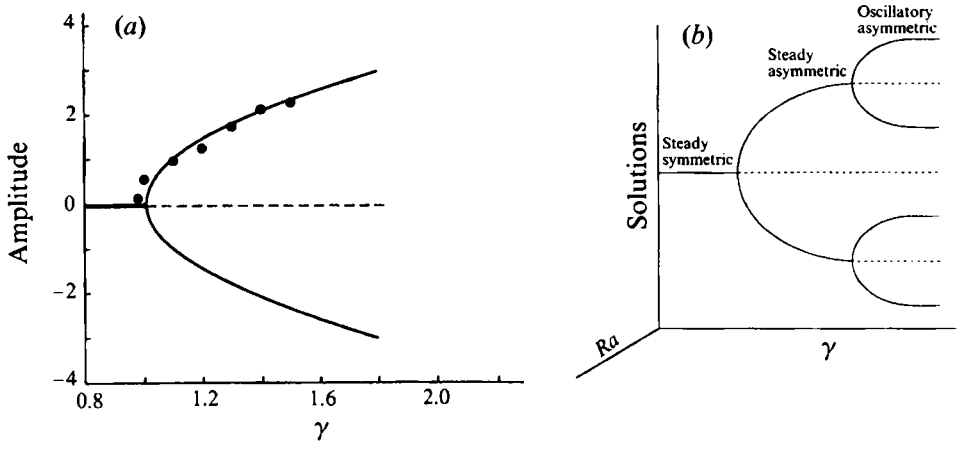

FIGURE 9. Bifurcation diagrams. (*a*) Computed Hopf bifurcation (see text for details); the fitted curve is $\gamma = 1.020 + 0.098A^2$. (*b*) Schematic bifurcation tree, showing how each asymmetric steady solution branch gives rise to a branch of oscillatory solutions having mirror symmetry with respect to each other.

In figure 9(*a*), the oscillatory amplitude A of the total kinetic energy is plotted against γ. The dots are from different numerical experiments and the smooth curve is the least-square fit of a parabola forced to be symmetric about $A = 0$. This follows the approach of Appendix C in QG for the pitchfork bifurcation studied there, in relying on the universal form of the amplitude *vs.* supercriticality curve near bifurcation (e.g. Ghil & Childress 1987, §12.2). A similar Hopf bifurcation occurs for the one-cell steady solution that has the plume near the left sidewall. The schematic diagram continuing the pitchfork bifurcation, studied in QG and in §§4.2 and 5.2 here, with the Hopf bifurcations studied in the present subsection appears in figure 9(*b*). Similar oscillatory states also exist for higher or lower Ra (not shown). As Ra is increased to 10^{12}, both the γ-value for pitchfork bifurcation (compare figure 14 in QG) and for Hopf bifurcation decrease. The general character of the sustained oscillations is similar to that at $Ra = 10^{11}$ (figures 7 and 8), but the flows are more vigorous and rapid. The bifurcation points with respect to γ for different Ra are expected to be different.

6. Type-B boundary conditions, $Ra_H = 10^5$

As defined at the end of §1, type-B boundary conditions mean either that the boundary values of T are monotonic in x and the boundary values of S are non-monotonic, or vice versa. In this section, we choose a monotonic T, cf. (2.6*e*), and a non-monotonic S, cf. (5.1), as being more realistic for the present-day North Atlantic (compare Weaver *et al.* 1993). Type-B boundary conditions eliminate the one-to-one correspondence between T and S, destroying their symmetry. Here we are interested in the following question: when a monotonic T is prescribed, how does an arbitrary non-monotonic S (and hence non-monotonic salt flux) affect the system? This condition is intermediate between monotonic and type-A boundary conditions. We wish to show that the details of the boundary values are not of crucial importance as far as large-scale flows are concerned. Regardless of these details, we should be able to generate symmetric and asymmetric steady flows, as well as oscillatory ones. As we shall see, dissimilar T and S restoring boundary conditions may, however, alter the stability

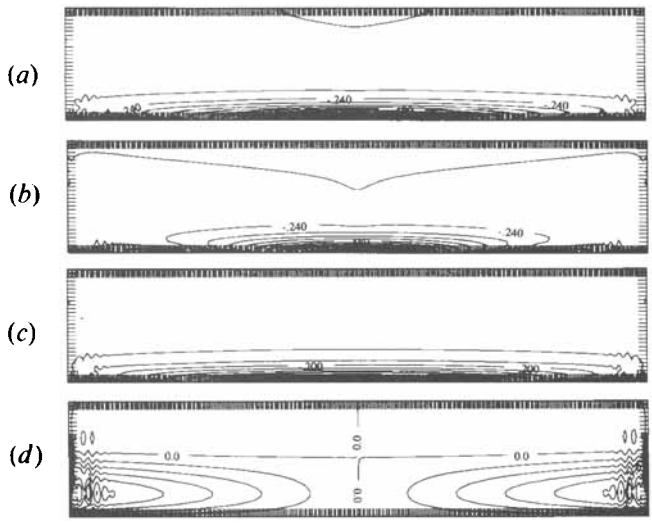

FIGURE 10. Symmetric steady state at $Ra = 10^{11}$, $\mathscr{P} = \mathscr{Q} = 0.01$, $\gamma = 1.0$, given type-B boundary conditions: (*a*) T; (*b*) S, $S_{min} = -0.96$, $S_{max} = 0$, $\Delta S = 0.06$; (*c*) $\rho, \rho_{min} = -0.65$, $\rho_{max} = 0.15$, $\Delta\rho = 0.05$; and (*d*) stream function, $\psi_{max} = 6.40$, $\Delta\psi = 0.80$.

properties of the system. We have chosen only one value of Ra for critical evaluation; this appears to be quite adequate for illustrative purposes.

6.1. *Symmetric steady solutions*

Figure 10 shows the steady-state contours of T, S, density anomaly and stream function, subject to restoring boundary conditions of type B, for $Ra = 10^{11}$. When the restoring boundary conditions for both T and S are the same, whether they be both monotonic or both non-monotonic, T, S, and the density field look exactly the same. Here, they all differ, as seen in figure 10(*a–c*). The better resemblance between T and the density indicates that the latter is much more strongly affected by T than by S. The flow field in figure 10(*d*) resembles that due to purely monotonic boundary conditions (figure 2*b*): the flow occupies only the lower half of the cavity; moreover, it has similar small-scale spatial oscillations near the sidewalls. However, the stream-function maximum here is almost 50% higher than that for the monotonic case, while being about 20% less than that for the type-A case in figure 4(*d*).

6.2. *Asymmetric steady and oscillatory solutions*, $\gamma = 2.0$ *and* $\gamma = 3.0$

Although type-B boundary conditions are in a sense intermediate between purely monotonic and type A, the results above indicate that temperature plays a more dominant role because $\gamma\lambda < 1$ (see §2). Both monotonic and type-A conditions led to similar types of solutions: symmetric equilibria give rise, via pitchfork bifurcation, to asymmetric equilibria that produce in turn, via Hopf bifurcation, oscillatory solutions. Hence, type-B boundary conditions should also produce all three types of solutions. Indeed they do, and the resulting solutions resemble in certain ways those of the other two cases, while in some ways they differ. In this subsection, we discuss briefly the flow configurations associated with type-B conditions, at $\gamma = 2.0$ and $\gamma = 3.0$.

The temporal evolution of the solutions, as well as the temperature and salinity fields, resemble the previous cases described in §§4 and 5. The run at $\gamma = 2.0$ was

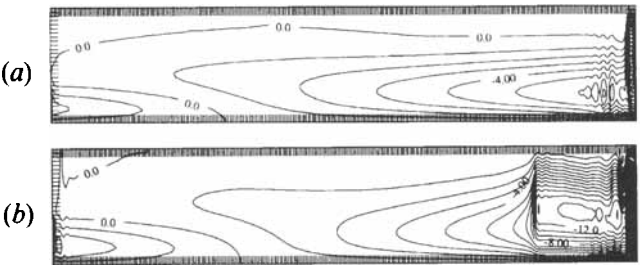

FIGURE 11. Stream-function contours for type-B conditions at $Ra = 10^{11}$, $\mathscr{P} = \mathscr{Q} = 0.01$: (*a*) asymmetric equilibrium at $\gamma = 2.0$, $\psi_{min} = -14.00$, $\psi_{max} = 5.00$, $\Delta\psi = 1.00$; (*b*) snapshot of oscillatory solution at $\gamma = 3.0$, $\psi_{min} = -26.00$, $\psi_{max} = 4.00$, $\Delta\psi = 1.00$.

carried out until the kinetic energy had reached a quasi-steady state, and the run at $\gamma = 3.0$ was carried out until an asymptotically oscillatory regime was reached. The flow fields of both solutions have a fairly permanent secondary cell in the lower-left corner. In figure 11(*a*) we show a quasi-steady asymmetric state with one cell being strongly dominant; in figure 11(*b*) we selected one time frame of an oscillatory solution, at the point at which the kinetic energy is near maximum. Figure 11(*a*) and figure 5(*a–c*) are quite similar except for the larger and stronger secondary cell here. The stream-function maximum is also larger than those in figure 5. Such differences are probably due to the values used for γ, rather than the difference in the boundary condition. Figure 11(*b*) can easily fit into the time series of figure 8(*a–h*). We have thus found no surprises in this set of intermediate boundary conditions. While a more complete exploration of the Ra–γ diagram for different types of boundary conditions does seem desirable, the shape of the boundary conditions is not crucial to the existence of either the first or the second bifurcation in the present two-dimensional Boussinesq system.

7. Concluding remarks

We have extended the study of thermosolutal convection of Quon & Ghil (1992, QG in the main text) to include small height-to-length aspect ratios δ and non-monotonic restoring boundary conditions. The non-monotonic restoring conditions of type A (both temperature and salinity non-monotonic) or type B (one monotonic and the other not) lead to non-monotonicity of the corresponding type in the derived mixed boundary conditions.

To produce convection-dominated flows for very small aspect ratios, one must use vertical components of viscosity and diffusivity that are much smaller than the horizontal components. Otherwise conduction dominates both the flow and solute transport even at (thermal) Rayleigh number Ra as high as 10^{11}, when Ra is based on the horizontal lengthscale L.

For aspect ratio $\delta \equiv H/L = 0.01$, we found that vertical-to-horizontal ratios of viscosity $\mathscr{P}$ and of diffusivity $\mathscr{Q}$ that are $O(\delta)$ yield convective flows for Ra-values of 10^{10}–10^{12}; the equivalent Rayleigh numbers based on height scale H are $Ra_H \equiv \delta^3 Ra = 10^4$–$10^6$. With salt-flux strength γ of order unity (between 1.0 and 2.0), the computations for all boundary conditions lead to an asymmetric steady-state circulation via a first bifurcation of pitchfork type; this circulation is restricted to or dominated by a single cell. Hopf bifurcation to oscillatory solutions is the second bifurcation found for all three types of boundary conditions, as γ is increased further, at $Ra = 10^{10}$, 10^{11} and 10^{12} ($Ra_H = 10^4$, 10^5 and 10^6). We have found,

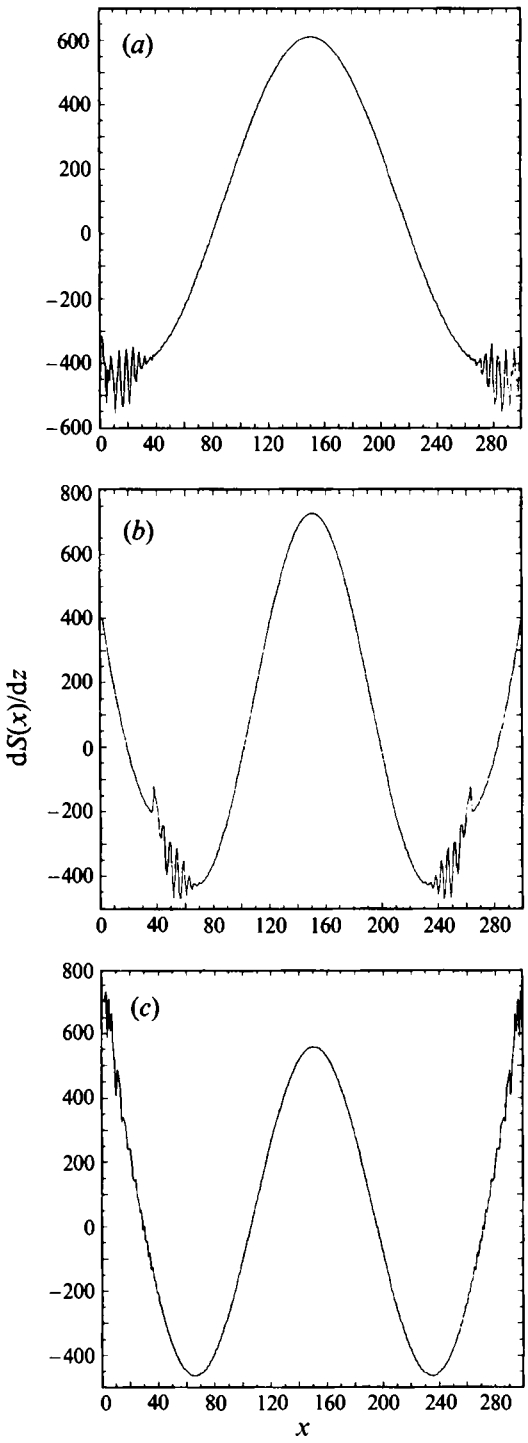

FIGURE 12. Salt flux computed across the bottom boundary for a steady symmetric state obtained with: (*a*) restoring monotonic boundary conditions in both temperature and salinity (the whole curve has been multiplied by a factor of 3, which is the value of γ used in the asymmetric computation of §6.2); (*b*) type-A non-monotonic boundary conditions; (*c*) type-B boundary conditions.

therewith, that Hopf bifurcation is extremely robust in the present two-dimensional Boussinesq system. It appears that type-A boundary conditions permit Hopf bifurcation at smaller γ.

It is found in our model that advective Hopf bifurcation is closely related to solitary wave-like disturbances generated in gravitationally unstable regions. Obviously, this result does not preclude Hopf bifurcation due to other dynamical mechanisms. It is clearly difficult to sort out all bifurcations mechanisms, let alone the model's complete Ra–γ regime diagram. To meet that objective, much more exhaustive studies need to be conducted. However, the studies we have carried out in QG and in this paper have identified some important criteria for bifurcation. We have gained valuable understanding of thermosolutal convection as thermal and trace-constituent flux are increased. To establish clear relations to physical phenomena observed in the world oceans will require more work at higher Rayleigh numbers, smaller $\mathscr{P}$ and $\mathscr{Q}$, and in three dimensions. Our work has nevertheless provided a stepping stone for further exploration of this complex and fundamental fluid-dynamics problem that might have some bearing on understanding the world's past and future climate.

The community of thermohaline circulation researchers is still small and its quest is young. Numerous discussions and exchanges of reprints and preprints have stimulated our continued interest in the problem and the work on this particular model. Support for this work from DOE Grant W/GEC0014 (through the National Institute for Global Environmental Change) and from an NSF Special Creativity Award to M.G. are gratefully acknowledged. B. Gola, K. Mah and C. Wong helped with the typing.

Appendix. Computed salt fluxes

Because the system is highly nonlinear, advective transport of tracers makes it difficult to predict what the salt flux will look like for a quasi-steady symmetric state obtained with given restoring boundary conditions. In figures 12(*a*)–12(*c*), we present the salt flux for monotonic boundary conditions, type-A and type-B non-monotonic boundary conditions, respectively. The latter two prescribed salt fluxes are non-monotonic in that they first decrease and then increase with distance from the midpoint of the enclosure along the x-axis, as does the prescribed temperature used in obtaining figure 12(*b*) (type-A boundary condition). The small-scale spatial oscillations are due to gravitational instability at steady state. It is obvious that these regions of instability are situated differently for the three cases.

It is interesting that in figures 12(*a*) and 12(*b*), the absolute salt-flux maxima are at the centre, while in figure 12(*c*) they are at the end points. For figure 12(*a*), obtained by prescribing monotonic temperature and salinity functions, decreasing from the vertical symmetry axis to the sidewalls, the result clearly indicates the dominance of the temperature effect (flow rising near the sidewalls and sinking near the centre) over the salinity effect (that tends to impose the opposite flow direction). The difference between figures 12(*b*) and 12(*c*), that agree in prescribed salinity (non-monotonic) but disagree in prescribed temperature (non-monotonic *vs.* monotonic), supports this conclusion.

REFERENCES

ALLEN, M. R., READ, P. L. & SMITH, L. A. 1992*a* Temperature time series? *Nature* **355**, 686.

ALLEN, M. R., READ, P. L. & SMITH, L. A. 1992*b* Temperature oscillations. *Nature* **359**, 679.

BRYAN, F. 1986 High-latitude salinity effects and interhemispheric thermohaline circulation. *Nature* **323**, 301–304.

BRYAN, K. & COX, M. D. 1968 A nonlinear model of an ocean driven by wind and differential heating. Parts I and II. *J. Atmos. Sci.* **25**, 945–978.

CESSI, P. & YOUNG, W. R. 1992 Multiple equilibria in two-dimensional thermohaline circulation. *J. Fluid Mech.* **241**, 291–309.

CHEN, F. & GHIL, M. 1995 Interdecadal variability of the thermohaline circulation and high-latitude surface fluxes. *J. Phys. Oceanogr.* (in the press).

GHIL, M., BENZI, R. & PARISI, G. (eds.) 1985 *Turbulence and Predictability in Geophysical Fluid Dynamics and Climate Dynamics.* North-Holland.

GHIL, M. & CHILDRESS, S. 1987 *Topics in Geophysical Fluid Dynamics: Atmospheric Dynamics, Dynamo Theory and Climate Dynamics.* Springer.

GHIL, M. & VAUTARD, R. 1991 Interdecadal oscillations and the warming trend in global temperature time series. *Nature* **350**, 324–327.

GREGG, M. C. 1987 Diapycnal mixing in a thermocline: A review. *J. Geophys. Res.* **92**, 5249–5286.

KAGAN, B. A. & MASLOVA, N. B. 1990 Multiple equilibria of the thermohaline circulation in a ventilated ocean model. *Ocean Modelling, issue* 90 (unpublished manuscript).

LEVITUS, S. 1982 Climatological Atlas of the World Ocean. *NOAA Professional Paper* 13. US Department of Commerce, National Oceanic and Atmospheric Administration.

MIKOLAJEWICZ, U. & MAIER-REIMER, E. 1990 Internal secular variability in an ocean general circulation model. *Climate Dyn.* **4**, 145–156.

QUON, C. & GHIL, M. 1992 Multiple equilibria in thermosolutal convection due to salt-flux boundary conditions. *J. Fluid Mech.* **245**, 449–483 (referred to herein as QG).

QUON, C. & SANDSTROM, H. 1990 A numerical algorithm to study internal solitary waves. *J. Comput. Phys.* **86**, 168–186.

SANDSTROM, H. & QUON, C. 1994 On time-dependent, two-layer flow over topography. II. Evolution and propagation of solitary waves. *Fluid Dyn. Res.* **13**, 197–215.

STOMMEL, H. 1961 Thermohaline convection with two stable regimes of flow. *Tellus* **13**, 224–228.

THUAL, O. & MCWILLIAMS, J. C. 1992 The catastrophe structure of thermohaline convection in a two-dimensional fluid model and a comparison with low-order box model. *Geophys. Astrophys. Fluid Dyn.* **64**, 67-95.

WALIN, G. 1985 The thermohaline circulation and the control of ice ages. *Paleogeogr., Paleoclimatol., Paleoecol.* **50**, 323–332.

WEAVER, A. J., SARACHIK, E. S. & MAROTZKE, J. 1991 Freshwater flux forcing of decadal and interdecadal oceanic variability. *Nature* **353**, 836–838.

WEAVER, A. J., MAROTZKE, J., CUMMINS, P. F. & SARACHIK, E. S. 1993 Stability and variability of the thermohaline circulation. *J. Phys. Oceanogr.* **23**, 39–60.